Mechanism of membrane perforation in rotavirus cell entry

Marilina de Sautu[1,2], Conny Leistner[3], Tomas Kirchhausen[4,5,6], Simon Jenni[1]*, Stephen C. Harrison[1,2,7]*

[1]Department of Biological Chemistry and Molecular Pharmacology, Harvard Medical School, Boston, Massachusetts, United States of America
[2]Laboratory of Molecular Medicine, Boston Children's Hospital, Boston, Massachusetts, United States of America
[3]Harvard cryo-EM Center for Structural Biology, Harvard Medical School, Boston, Massachusetts, United States of America
[4]Department of Cell Biology, Harvard Medical School, Boston, Massachusetts, United States of America
[5]Department of Pediatrics, Harvard Medical School, Boston, Massachusetts, United States of America
[6]Program in Cellular and Molecular Medicine Boston Children's Hospital, Boston, Massachusetts, United States of America
[7]Howard Hughes Medical Institute, Harvard Medical School, Boston, Massachusetts, United States of America

*Correspondence: jenni@crystal.harvard.edu, harrison@crystal.harvard.edu

ABSTRACT

Infectious cell entry by non-enveloped viruses requires delivery of the viral genome -- in many cases enclosed within a large, subviral particle -- across the membrane of an intracellular compartment. Rotaviruses and other double-strand RNA (dsRNA) viruses introduce into their target cells an inner capsid particle, roughly 700 Å in diameter, that does not uncoat further but instead extrudes capped viral mRNA by virtue of RNA-dependent RNA polymerase and capping activities within it. The delivery agent is an outer protein layer of the virion. We describe here use of cryogenic electron tomography (cryo-ET) to visualize the full course of rhesus rotavirus (RRV) entry, from cell attachment and inward budding of the virion to arrival of the subviral particle in the cytosol. The cryo-tomograms and subtomogram averaging of classified subparticles have enabled us to link high-resolution structures of the virion and its components with time series from live-cell fluorescence microscopy and thus to outline

the molecular mechanism of each step in the entry process, including the hitherto elusive membrane perforation step needed for transfer of the subviral particle into the cytosol.

INTRODUCTION

Rotaviruses, so named for their "wagon-wheel" like appearance in the electron microscope, are a group of non-enveloped viruses with segmented, double-strand RNA (dsRNA) genomes [1]. The outer layer of an infectious rotavirus particle ("triple-layer particle": TLP) comprises two proteins – a spike-like asymmetric trimer (VP4, magenta, red, orange and tan, in Figs. 1a,b) and a Ca^{2+}-stabilized trimer (VP7, yellow, in Fig. 1a) [2-4]. The role of the outer layer is to deliver the double-layer particle (DLP) it surrounds into the cell to be infected. A maturation proteolytic cleavage processes VP4 into VP8* (magenta) and VP5* (red, orange, tan), with excision of a few residues at the junction and loss of all but the N-terminal 26 residues of VP8* from one of the three subunits (Fig. 1b). Within the DLP, VP1, the RNA-dependent, RNA polymerase (RdRp), associated 1:1 with each dsRNA segment, generates messages, capped by the activity of VP3, a guanylyl- and methyl-transferase, and extrudes them co-transcriptionally without further uncoating [1, 5-9]. VP4, cleaved to VP8* and VP5*, mediates both attachment and uptake of a TLP. VP8* binds the receptor – sialic acid on glycolipids, in the case of the rhesus rotavirus (RRV) used in the studies reported here, and blood-group antigens for certain human rotaviruses [10, 11]. VP5* then engages the membrane through hydrophobic loops at the tip of its prominent β-barrel domain and undergoes a conformational change that inserts its C-terminal, "foot" domain into the target membrane (Fig. 1b) [4]. These interactions drive membrane invagination, which we know, from our previous work on RRV entering BSC-1 cells, is a largely self-driven, dynamin-independent, endocytic process, potentially assisted at late stages of pinching off by the activity of cortical actin [4, 12-14].

In experiments in which each of the components (VP4, VP7, DLP) was marked with a spectrally distinct fluorophore, we traced a trajectory from attachment to DLP delivery into the cytosol over a time course of no more than 10–15 min [12, 15, 16]. An initial step after complete engulfment of a particle (i.e., pinching off of a virion-containing vesicle) is loss of Ca^{2+} from the particle and from the vesicle containing it [15]. Permeabilization of the membrane to Ca^{2+} is a consequence of VP5* foot insertion, so that Ca^{2+} equilibrates with the cytosol once pinching off is complete [13]. VP7, a Ca^{2+} stabilized trimer, then loses Ca^{2+} and dissociates from the particle [3, 17].

In the work reported here, we have defined the molecular steps just described by combining live-cell imaging, high-resolution structures, and single molecule-format assays. Cryo-ET of cells immediately after incubation with TLPs, which has now enabled us to visualize entry directly, indicates that VP7, as a dissociated monomer, is the protein that opens up the vesicular membrane and permits the DLP to escape into the cytosol. We confirm this VP7 activity by experiments with liposomes in vitro. Our model for the activity – projection of an amphipathic helix shown previously to perforate liposomes – suggests a mechanism with potential significance for other non-enveloped viruses.

RESULTS

Cryo-ET visualization of rotavirus entry

We recorded tilt series of rotavirus entering from the periphery of BSC-1 cells, which spread enough not to require further thinning by FIB-milling (Fig. 1c). TLPs were added to cells on grids at 37 °C, allowed to bind for 10 min before exchange of medium, and incubated for 10 more min before plunge freezing (Fig. S1). Fig. 1d and Movie S1 show a representative tomogram and molecular segmentation of the BSC-1 cell periphery. The analysis that follows included 838 tomograms from 7 separate experiments (datasets 1–7, Table S1). Figs. 2a–f show representative tomographic slices of various entry stages together with their interpretation based on subtomogram averaging, local classification of virus structure and conformation, segmentation of cellular membranes, and identification of relevant cellular components. The description here comes from images in which just one or two particles are present in the same endocytic vesicle, so that the conclusions can correspond to our published live-cell imaging experiments, in which all traces had initial intensities corresponding to calibrated labeling for single virions [12].

Fig. 2a illustrates that particles interact with cell membrane through their VP4 spikes in two distinct contact modes, as we have shown previously [4]. In the “loose” contact, the spike engages the membrane through the VP8* lectin domains, which bind a glycosphingolipid sialic acid group. In the “close” contact, which reflects the spike conformational transition from “upright” to “reversed”, the VP5* hydrophobic loops contact the outer leaflet of the membrane bilayer, into which the foot domain inserts. Fig. 2b shows that wrapping of membrane around the particle appears to require the strong close contacts; fully internalized particles usually have a large part of their surface in close contact with vesicular membrane (Figs. 2b,c). Our published work also shows that these reversed contacts allow Ca^{2+} to traverse the membrane [13].

Once fully engulfed, the TLP loses Ca^{2+} as the ions pass from the endocytic vesicle lumen into the low-Ca^{2+} environment of the cytosol and VP7-bound Ca^{2+} ions dissociate. Figs. 2c,d show that VP7 dissociation ("uncoating") occurs on the side of the particle distal to the membrane-contacting surface, indicating that uncoating initiates away from the site of attachment. Even after membrane perforation and extensive VP7 dissociation, residual VP7 sometimes remains on one side of the largely uncoated particle (Fig. 2d, black arrows). Thus, despite generating a Ca^{2+} leak, insertion of reversed VP5* into the membrane evidently stabilizes the outer layer in the region of close contact.

Figs. 2d,e show various examples of membrane rupture with escaping DLPs. From live-cell imaging experiments [12, 15, 16], we know that escaping particles diffuse rapidly away from the vesicle they leave, consistent with the relatively few examples of the exit step captured in our dataset. The frames illustrated here show that a single, large aperture opens up in the vesicular membrane, rather than a general, multi-point dissolution of the bilayer. The fuzzy decoration of the pore rim (e.g., white arrow in Fig. 2d) suggests that the scission event requires stabilization of the exposed edges of the bilayer by the dissociated VP7, as described in the following section. DLPs that escape into the cytosol are often surrounded by clusters of ribosomes (Fig. 1f), suggesting immediate translation of the emerging transcripts.

VP5* membrane interaction

From seven datasets, each corresponding to a session on a Titan Krios G3i electron microscope, we found positions of virus particles by 3D template matching [18] in 537 of the 838 acquired tomograms. We selected 8,565 particles for icosahedral subtomogram averaging and refined their positions and orientations with RELION [19] and M [20] (see Methods). After tilt series refinement in M, we reached a final resolution for a reconstructed particle of 4.7 Å (Fig. S2 and Table S1). We then symmetry-expanded the particles and extracted 3D subparticles corresponding to individual VP4 spike positions. 3D classification in RELION [19] partitioned the 513,900 subparticles into three main classes, corresponding to 58% upright and 11% reversed spike conformations, and to 31% unoccupied ("empty") spike positions (Fig. S3 and S4). We also segmented all membranes in tomograms using MemBrain [21, 22] and calculated the value for an overlap factor between each spike location and segmented membrane (see Methods and Fig. S5a–d). Viruses with high membrane overlap had extensive close contacts (Fig. S5e,f), and the spikes that classified as reversed showed on average substantially higher membrane overlap than did the upright ones (Fig. S5g–j and Data S1), confirming that the VP5* conformational change from upright to reversed correlates with membrane interaction. We also calculated the distance of segmented membrane (from the center of the virus) at spike

positions (see Methods), and the distribution shifted from loose to close spacings between upright and reversed, respectively (Fig. S6a,b).

We used the overlap factor to select membrane-engaged, reversed-conformation VP5*, shifted the box to the center of the spike, and performed 3D classification with C_3 symmetry imposed (Fig. 3a). After classification with either a wide or tight mask, 3D maps reconstructed in M (Fig. S7) showed the VP5* β-barrel trimer, characteristic of the reversed conformation, with a central three-chain coiled-coil domain that extends through the membrane (Fig. 3a). The reversed-spike structure (PDB-ID 9C1J) could be docked with confidence into the map. The rotational density average calculated from 42 viruses with high membrane overlap and close contact with vesicular membrane over almost their full circumference suggests that the midpoint of the lipid bilayer bound to reversed VP5* spikes is at about 443 Å from the center of the particle (Fig. 3b,c). The membrane boundaries shown in Fig. 3a are estimated from the rotational density average (Fig. 3c). The tips of the VP5* hydrophobic loops insert into the proximal leaflet of the bilayer, and the three-chain coiled-coil extends across the bilayer's hydrophobic core (Fig. 3a). Our published high-resolution structures show that the distal part of the coiled-coil in the reversed conformation includes most of the initial α helix of the "foot" domain in the upright conformation [2, 4, 23]. Three globular features that likely represent the rest of the "foot" polypeptide chain splay symmetrically away from the coiled-coil at a level corresponding to the cytosolic-side polar headgroups of the membrane bilayer (Fig. 3a).

Uniform close contacts between entering TLPs and the invaginating plasma membrane show that the coiled-coil and foot of VP5* insert into the membrane as inward budding proceeds, thus generating the work needed to distort the bilayer and wrap it tightly around the particle (Fig. 2b). The same membrane insertion also results in Ca^{2+} permeability [13], and we therefore expect Ca^{2+} to enter the cell from the medium even during the engulfment process. Imaging of cells transfected with GCaMP6s-CAAX, a plasma membrane targeted Ca^{2+} sensor [24], detects the expected Ca^{2+} concentration transients during short incubation with rotavirus particles (Fig. S8).

In most of our tomograms, the vesicle that results from pinching off of the wrapped membrane has an ovoid aspect – close contacts are present over at least one side of the TLP but the distal surface faces a small volume of enclosed medium (Fig. 2b,c). This property of the budded vesicles suggests that pinching off requires some cellular mechanical activity -- most likely local mobilization of cortical actin, as indicated by reduced efficiency of infection in the presence of latrunculin A (Fig. S9a). One potential functional consequence of Ca^{2+} permeation as the vesicle forms is reorganization of actin close to the entering TLP, by Arp2/3 activation as a downstream consequence of Ca^{2+} signaling. Inspection of actin

filaments in the vicinity of entering particles shows that unlike the arrangement of cortical actin parallel to the membrane in regions lacking adsorbed virions (Fig. S9b,c), actin at sites of entry forms branched networks surrounding the viral invaginations (Fig. S9d,e). Manual segmentation of actin filaments in networks surrounding individual particles illustrates their three-dimensional character, which corresponds well to the geometry expected of Arp-2,3-mediated nucleation (Fig. S9f,g).

Liposome disruption by VP7 monomer

We can detect VP7 dissociation by the loss of the thin, wagon-wheel rim of the particle (Fig. 2d). Within a vesicle, VP7 dissociation proceeds distal to the close membrane contact; extensive uncoating correlates with membrane rupture and particle escape into the cytosol (Fig. 2d). These observations suggest that dissociation of monomeric VP7 from virus particles during uncoating, triggered by Ca^{2+} depletion within the vesicle, has a role in membrane disruption and facilitates particle escape. We estimate that when about 50% of the 780 copies of VP7 on a particle has dissociated (nearly 400 monomers), the free VP7 concentration within a typical vesicle (e.g., as in Fig. 2b,c) will be approximately 1 mM. We tested whether VP7 monomers or trimers, without contribution of any cellular factor, could disrupt a liposome membrane and induce release of an encapsulated fluorescent dye. We incorporated carboxyfluorescein (CF) into liposomes containing a fluorescently labeled lipid (Cy5-DOPE) in the bilayer and a biotinylated lipid for attachment to a biotinylated-PEG coated coverslip by avidin (Fig. 4a). The lipid composition was similar to that of mammalian plasma membranes. We recorded by total internal reflection fluorescence (TIRF) microscopy 30-min time lapse movies of coverslip-anchored liposomes, following addition of either EDTA buffer alone, VP7 trimer in Ca^{2+} buffer, or VP7 monomer in EDTA buffer. The intensities of the diffraction-limited spots in the two recorded channels, at 488 nm and 640 nm, reflected the presence of liposomes and their CF content, respectively. Time-lapse images of the same field of view showed that in the presence of VP7 monomer in EDTA buffer, the CF signal often disappeared abruptly while the lipid signal persisted, indicating membrane perforation that had allowed dye to leak from the liposomes (Fig. 4b). At 30 min after adding VP7 monomer, about a third of the liposomes had lost more than 50% of their initial CF signal, while no significant CF signal loss occurred when liposomes were incubated with VP7 trimer in Ca^{2+} buffer or with EDTA buffer alone (Fig. 4c and Fig. S10). Incomplete loss of CF indicated either a multilamellar liposome or two unresolved, adjacent liposomes. Cryo-EM images of the same liposome preparations showed localized perforations (Fig. 4d and Fig. S11) that recapitulated the site-specific vesicle disruption patterns observed in infected cells by cryo-ET (Fig. 2d,e; Fig. 4e).

Early experiments, using a bulk assay to monitor liposome disruption by VP7, showed activity from a peptide close to the C terminus of the VP7 polypeptide chain, W292–K312 (Fig. 4f), released from the

protein by adventitious proteolytic cleavage [25]. The assay used in those experiments, of lower sensitivity than that of the single-liposome assay used here, did not detect disruption when using intact, uncleaved VP7 monomer. Liposome disruption by a similar, 21-residue, synthetic peptide (Q280–M310) was later also described [26]. As a specific precaution to avoid proteolysis, we added trypsin inhibitor to the single liposome experiments described above.

In the VP7 trimer, residues W292–K312 (orange, in Fig. 4f) form a kinked helix at the Ca^{2+}-dependent interface, with one of the Ca^{2+} ligands (D310) near its C terminus. If straightened, W292–K312, would form a perfectly amphipathic, ~30 Å-long α helix. We suggest that the kinked helix can unfold and straighten when not constrained by its Ca^{2+}-stabilized contacts in the trimer (Fig. 4f). The proteolytic sensitivity of the R291-W292 peptide bond, but only when the trimer dissociates, exposes the interface, and liberates the helix in question, is good evidence for flexibility near R291 (Fig. 4f). In cell entry, the high local concentration of monomeric VP7 in the vesicle will favor interaction of this amphipathic helix with the lumenal membrane leaflet of the vesicle. We discuss below the transition from amphipathic binding to large pore formation. The synthetic VP7 peptide ($VP7^{292-312}$) produced localized perforations in single liposomes very similar to those observed by intact VP7 monomer (Fig. 4d), consistent with a mechanism in which the corresponding segment projects from the folded VP7 globular structure.

Rotavirus infection in vertebrate hosts occurs in the trypsin-rich lumen of the proximal gut. We considered whether inclusion of traces of trypsin within the endocytic vesicle generated by the entering virus might release the membrane-disrupting, C-terminal peptide from monomeric VP7 dissociated from the Ca^{2+}-depleted particle. We therefore carried out an infectivity assay in the presence of either small amounts of trypsin or of trypsin inhibitor and found no significant infectivity difference (Fig. S12). We conclude that release by tryptic cleavage of the amphipathic VP7 peptide is not required for rotavirus infection to proceed.

DISCUSSION

Our results (Fig. 2) lead to the following inferences, consistent with the kinetics we have established by live-cell imaging [12, 15, 16]. (1) Binding of RRV TLPs at the surface of BSC-1 cells relies on the upright conformation of VP4 ("loose" contacts with the cell surface), but invagination and final engulfment rely on the reversed conformation ("close contacts"). Insertion of the C-terminal part of VP5* (coiled-coil and foot) into the plasma-membrane bilayer, thereby generating the close contacts, provides the free energy needed to wrap membrane around the particle. We detect no features that might be ascribed to a protein receptor. (2) VP5* insertion, which permeabilizes a membrane to Ca^{2+} [13], allows Ca^{2+} ions to

enter the cell, leading to downstream Ca^{2+} signaling and likely to local reorganization of the actin cytoskeleton, facilitating closure of the vesicle that surrounds the entering TLP. (3) Vesicle closure allows depletion of Ca^{2+} within it, as there is no longer replenishment from the medium, initiating VP7 dissociation. (4) Dissociation is distal to the close membrane contacts, which appear to stabilize the VP7 layer, even though the Ca^{2+} flux is through the reversed VP5* spikes within the close contact. (5) Dissociated VP7 monomers are therefore the presumptive agents of membrane perforation. (6) In vitro, monomeric VP7 disrupts liposomes and forms single, large pores that resemble the DLP exit pores captured by cryo-ET. A peptide spanning residues 292–312 of VP7 forms similar pores in vitro. (7) Ribosomes often surround the DLPs released into the cytosol, suggesting translation of nascent viral mRNA as it exits the transcriptionally active DLP.

The sequence corresponding to VP7 residues 292–312 in RRV is conserved among rotavirus A strains; in the other groups, it varies somewhat more than among group A strains, but it retains both amphipathicity and a potential aspartate Ca^{2+} ligand. We have pointed out in previous papers that rotavirus entry through clathrin-mediated endocytosis might in principle be an infectious pathway in other cell types or for other rotavirus strains. Clathrin dissociates within a minute of pinching off [27], and the resulting uncoated vesicle would be nearly indistinguishable from the small vesicles from which RRV DLPs penetrate in BSC-1 cells. VP5* insertion could occur either during coated pit assembly or after clathrin uncoating. Ca^{2+} loss, and VP7 dissociation would then follow as seen here.

The entry mechanism illustrated by our data includes two distinct membrane-insertion events. The first accompanies the upright-to-reversed conformational transition of VP5*; the second is perforation by VP7. A likely mechanism for VP5* insertion is one in which the VP8* lectin domains first dissociate from the hydrophobic tips of the VP5* β barrels [28]. The dissociation can be spontaneous, as the interface between VP8* and VP5* is quite small, but VP8* cannot fully dissociate because of the tether that connects the lectin domain at the tip of the spike to the N terminus of the VP8* polypeptide chain, well anchored in the foot (see magenta helices in Fig, 1b). That is, the lectin domain is probably always in an "on-off" equilibrium, and when not attached to membrane, it will reassociate promptly. When the lectin domain binds a glycolipid headgroup, however, its dissociation can allow the hydrophobic tips of the β barrels to engage the membrane, preventing reassociation and initiating the upright-to-reversed conformational change. Zippering up of the central coiled-coil will extract the unfolding foot from beneath the VP7 layer and project it through the bilayer. The model for membrane-inserted VP5* we obtained by sub-tomogram averaging (Fig. 3a) represents the result of this transition. Although of limited resolution, the model suggests a potential axial channel through which Ca^{2+} might pass: the coiled-coil density appears to splay apart as it enters the bilayer and to terminate in connections to the radially

projecting globular densities we ascribe to the extruded foot. Confident definition of a Ca^{2+} pathway will require a higher-resolution density map.

The mechanism of DLP release now visualized by cryo-ET is consistent with our published findings that crosslinking of VP7 subunits within a trimer, either by divalent antibodies or by mutationally introduced disulfides, inhibits infection and prevents concomitant entry of the toxin, α-sarcin [29]. Because DLP transcriptional activity requires VP7 [30], those observations did not by themselves imply that VP7 has perforating activity and left open the possibility that VP5* or a combination of VP5* and VP7 disrupted the membrane. It is now clear that loss of Ca^{2+} through the VP5*-generated leak, which destabilizes the VP7 trimer and causes it to dissociate from the particle, leads both to activation of the DLP as a transcriptase and to generation of the VP7 monomer as a pore-former.

The VP7-generated pores have several noteworthy features, both in the cryo-tomograms (Fig. 2d,e) and in the liposomes in vitro (Fig. 4d). (1) There is always a single pore per vesicle/liposome, of variable size *in vitro* and probably in cells; (2) the fuzzy edges of the pores show that many copies of VP7 line the rim; (3) the membrane bilayer curves outward at the rim of the pore, so that the plane of the bilayer edge is roughly normal to the pore axis (Fig. 4 d,e). The presence of a single pore per vesicle/liposome indicates cooperativity, and the variable size is compatible with an initiation-growth mechanism. Growth could potentially be fed by association of the amphipathic helix with the membrane surface. Unlike the large, β-barrel pores of cholesterol-dependent toxins such as perfringolysin O, there is no pre-pore ring [31]. Proposals for pore formation by amphipathic helices lead either to a "barrel-stave" arrangement, in which the helices, approximately normal to the plane of the membrane, form a barrel that defines the circumference of the pore, with hydrophobic residues facing the fatty-acyl chains and hydrophilic residues facing the aqueous channel [32, 33], or to a related alternative, a "toroidal pore", in which the helices are not in tight lateral contact, and lipid headgroups project between them, as at the edges of a bicelle [34]. It is possible that the VP7 perforations initiate as barrel-stave or toroidal pores, with the rim turning outward as the pore grows, but our current structural data are not of sufficient resolution or contrast to show early events. Cryo-EM images of pores induced in mitochondrial outer membranes and liposomes by the pro-apoptotic protein Bax are very similar to those in Fig. 4d [35, 36], but most models for pore formation by Bax and related proteins involve association of globular domains along with insertion of an amphipathic peptide [37, 38]. Similar apparent pore structures from intact VP7 monomers and amphipathic peptide alone rule out such interactions for the perforations seen here. To cover the rim of a pore 100–120 nm in diameter with close contacts between helices – roughly the size of the perforations we see in our tomograms – would require 300–350 helices – i.e., participation of less than half of the 780 total VP7 monomers on a rotavirus particle (Fig. 4e). Thus, the available VP7

can readily form the observed openings. Moreover, our estimate of 1 mM, for the concentration of VP7 monomers in the vesicle, is consistent with a rapid association with membrane, as required by the short delay between loss of Ca^{2+} and onset of vesicle perforation [15].

A feature of our tomograms probably important for the observed perforation mechanism is the relatively small volume of the vesicle from which the DLP escapes. Were the dissociated VP7 diluted into a much larger volume, its concentration might be insufficient for rapid, cooperative formation of a single, large pore. Thus, if related perforation mechanisms apply to other non-enveloped viruses that deliver a modified virion into the cytosol, they may likewise occur in small compartments soon after uptake. For example, an amphipathic helix at the N terminus of adenovirus protein VI is essential for translocation of an infecting adenovirus particle from an early endosome into the cytosol, after loss of pentons and peripentonal hexons (induced by lowered pH) and release of internal components including pVI [39-42]. Early endosomes vary in size, but those at the smaller end of the range are comparable to the vesicles from which we see escape of RRV.

METHODS

Cells, plasmids and constructs

MA104 cells (ATCC) were grown in medium 199 Earle's salts (M199, Thermo Fisher Scientific) supplemented with 25 mM 4-(2-hydroxyethyl)-1-piperazineethanesulfonic acid (HEPES) and 10% Hi-FBS (Thermo Fisher Scientific). BSC-1 cells (ATTC) were grown in Dulbecco's Modified Eagle Medium (DMEM) with GlutaMAX (Thermo Fisher Scientific) supplemented with 10% Hi-FBS (Thermo Fisher Scientific). For VP7 expression, we cloned the full-length VP7 genomic sequence (G3 serotype, NCBI: txid444185) into a pFastbac expression vector, which we transformed into *E. coli* DH10α cells. For bacmid generation, VP7 vectors were transformed into DH10-Bac cells (Thermo Fisher Scientific) and plated onto LB-agar plates supplemented with 50 µg/ml kanamycin, 7 µg/ml gentamycin, 10 µg/ml tetracycline, 100 µg/ml blue-gal and 40 µg/ml β-D-1-thiogalactopyranoside (IPTG).

Reagent preparation

Purification of rotavirus TLPs – MA104 cells were grown to confluency in 850 cm^2 roller bottles in M199 supplemented with 10% FBS and 25 mM HEPES. Cells were infected with rhesus rotavirus (RRV, strain G3P5B[3]) at a multiplicity of infection (MOI) of 0.1 with 5 µg/ml of trypsin in the medium. After incubation at 37 °C for 24 h, the medium containing cells and debris was collected and frozen at -80 °C. After thawing, cells and debris were pelleted by centrifugation in a Beckman Coulter rotor JS 4.2 at 2,900 g for 30 min at 4 °C. Supernatant was then removed and the pellet resuspended in 1 ml ice cold TNC

buffer (20 mM Tris, 100 mM NaCl, 1 mM $CaCl_2$, pH 8.0). Virus particles were concentrated from the supernatant by ultracentrifugation in a Beckman Coulter rotor Ti-45 rotor at 224,500 g. The supernatant was then discarded, and the pellet was resuspended in 1–3 ml ice cold TNC buffer and combined with the cell-debris fraction from the first centrifugation. The suspension was transferred to a 15 ml conical tube, and TNC was added to a final volume of 4 ml. The suspension was mixed with 4 ml of 1,1,2-trichloro-1,2,2-trifluoroethane (Freon 113) by tube inversion 5–10 times, sonicated for 15 seconds (0.5s on, 0.5s off) at 11% amplitude on a Branson Digital Sonifier in the cold room and centrifuged for 10 min in a Beckman Coulter rotor SX4750 at 200 g at 4 °C. The upper aqueous phase was removed and transferred to a new clean 15 ml conical tube, and the Freon extraction was repeated two more times. The resulting virus solution was divided in aliquots of 500 μl and layered on top of a 35–60.0% (w/v) CsCl gradient (1.26–1.45 g/ml) prepared in six SW60 tubes. CsCl solutions were prepared in TNC. Gradients were spun at 4 °C in a Beckman Coulter rotor SW 60 at 406,000 g for 2.5 h. Bands for TLPs and DLPs were harvested by side puncture. TLPs and DLPs were dialyzed against 2 L of TNC or TNE overnight. Virus particles were concentrated by pelleting at 4 °C in a Beckman Coulter rotor SW 60 at 406,000 g for 1 h. Supernatants were removed carefully, and pellets resuspended in 100–200 µl of remaining buffer. TLP concentration was measured by densitometry of VP6 bands on Coomassie stained SDS-PAGE gels against DLP standards ranging from 0.1 to 1.0 mg/ml.

Purification of recombinant VP7 – Baculovirus vectors carrying the genetic information of full-length rhesus rotavirus VP7 (G3 serotype) were produced from bacmid transfected Sf9 cells (Thermo Fisher Scientific). The viruses were then inoculated into fresh Sf9 cells grown on T25 flasks and passaged three times with an incubation time of 72 h for each passage. Eight glass spinner flasks with 500 ml of Sf9 cells with approximately 2 million cells per ml were then infected with 13 ml of passaged virus stock solution and incubated for 72 h. Cells were harvested at 4 °C by centrifugation in Beckman Coulter rotor J 4.2 at 3500 g for 30 min. Purification was performed as previously described [3], with minor modifications. The supernatant was collected and benzamidine and sodium azide were added to final concentrations of 1 mM and 0.01% (w/v), respectively. Supernatant was loaded into 50 ml of a concanavalin A Sepharose (ConA) resin. Resin was washed with five column volumes (CV) of TNC buffer. Protein was eluted with five column volumes of TNC buffer containing 0.6 M α-methyl mannose. The eluate was then loaded onto 11 ml protein A resin with immobilized antibody m159 [43] (10 mg per ml of protein A resin), specific for trimeric VP7, and equilibrated in 20 mM Tris, 50 mM NaCl, 0.1 mM $CaCl_2$, pH 8.0. We washed bound VP7 protein with five CV of buffer and eluted with five CV of 20 mM Tris, 50 mM NaCl, 1 mM EDTA, pH 8.0. Buffer was exchanged by overnight dialysis in 0.1HNC (2 mM HEPES, 10 mM NaCl, 0.1 mM $CaCl_2$). Protein was frozen in liquid nitrogen and stored at -80 °C.

Cryo-ET data collection and processing

Grid preparation – BSC-1 cells were cultured overnight on 200-gold mesh Quantifoil grids (2/2) with SiO_2 previously incubated for 4 h with 1 mg/ml fibronectin (Corning). RRV, strain G3P5B[3], at 0.034 mg/ml was added and incubated for 10 min. The grids were then washed with medium and incubated for an additional 10–20 min. Samples were vitrified in liquid ethane using a Leica EM GP plunge freezer. Cell distribution was assessed by scanning electron microscopy (SEM) on a Thermo Fisher Scientific Aquilos 2 (Fig. S1).

Tomographic tilt series collection – Tilt series, imaging at the thin cell periphery, were acquired on a Thermo Fisher Scientific Titan Krios G3i equipped with a Falcon 4i detector and a Selectris energy filter (10 eV slit width). Data were collected following a dose-symmetric bidirectional tilt scheme [44], with a nominal defocus range of -3 to -5 µm. Tilt angles spanned from +60° to -60° in 3° increments, yielding 41 tilts per series. Each tilt was acquired at a dose of 3.7–3.9 electrons per $Å^2$, for a total cumulative dose of ~150 electrons per $Å^2$. Four frames were recorded per tilt image. A total of 838 tilt series were acquired across seven datasets (Table S1).

Initial tomographic tilt series processing – Tilt image movie frames were aligned and averaged with WarpTools version warp_2.0.0dev29 (fs_motion, grid 1×1×5) and used for contrast transfer function (CTF) parameter estimation (fs_ctf, grid 2×2×1) [45]. To exclude bad tilt images from downstream processing, we calculated the pixel value distributions from the tilt image averages using IMOD (clip histogram -F 0.5,1) [46] and excluded bad tilt images from the corresponding mdoc files based on pathologic falloff of the density histograms. We made tilt series image stacks with WarpTools (ts_stack) and then used AreTomo2 version 1.1.2 [47] for initial tomographic alignment (VolZ 4400, AlignZ 1400). Alignments were imported with WarpTools (ts_import_alignments), and the handedness of the CTF model was checked (ts_defocus_hand) before fitting it for the entire tilt series (ts_ctf). We then reconstructed 4×- (~9.4 Å per pixel) and 8×-binned (~18.8 Å per pixel) tomograms with WarpTools (ts_reconstruct).

Rotavirus particle picking (3D template matching) – With e2spt_tempmatch.py from EMAN2 [48], we located rotavirus particles in the 4×-binned tomograms (~9.40 Å per pixel), using a previously determined icosahedrally averaged cryo-EM reconstruction of the rotavirus TLP (EMD-45118) scaled to the correct pixel size. We imposed I_2 symmetry in the computation and kept particles with a score above a defined threshold (vthr 8.0). We extracted 4×-binned 3D subtomograms with WarpTools (ts_export_particles, box 128), calculated low pass filtered 2D projections with RELION (relion_project)

[49] for visualization and manual exclusion of false picks. See Table S1 for the number of particles from each dataset.

Initial subtomogram alignment – After extracting 2×-binned (~4.70 Å per pixel) 3D subtomograms and corresponding 3D CTF volumes with WarpTools (ts_export_particles, box 256), we used RELION (relion_refine) for reference-based subtomogram alignment. This step was redundant, as alignment parameters were in principle already obtained from the EMAN2 particle picking, but we included the step because e2spt tempmatch.py did not output the alignment angles. The alignment-angle convention is the same in Warp/M and RELION. Alignment and reconstruction were done with I_2 symmetry imposed, and the reference was masked with a spherical mask, outer radius 512 Å.

Tomographic tilt series refinement – We used M (MCore, version warp_2.0.0dev29) for tomographic tilt series refinement [20]. We created a population with a single species (as defined by Warp/M) based on the previously located and aligned rotavirus particles. The box was 512 cubic pixels (unbinned data) at ~2.35 Å per pixel (Table S1). As mask, we used a low-resolution envelope of the three protein layers (VP2, VP6, VP7) and the VP4 spikes in upright conformation. Several iterations of M refinement were carried out with I_2 symmetry imposed and with a sequential increase in the complexity of the distortion model (image warp, particle poses, stage angles, volume warp, defocus, tilt movie refinement, magnification distortion, CTF refinement). We did the final refinement rounds after fitting weights per tilt series and fine-sampling the trajectories of the particle poses to 3. We determined the true pixel size for each dataset (Table S1) by scaling the final reconstruction to a reference, a previously determined cryo-EM reconstruction of the virus at 2.36 Å resolution (EMD-45118) (Fig. S2a). The Fourier shell correlation (FSC) curves calculated from the half maps for the icosahedral reconstructions of the 7 datasets are shown in Fig. S2b. We also compared the reconstructions to a “perfect” model, the 2.36 Å cryo-EM reconstruction (EMD-45118), in order to assess the extent of fitted noise after tilt series refinement (Fig. S2c). The variation in the observed resolution between reconstructions from different datasets (ranging from to 4.7 [Nyquist] to 8.8 Å, Table S1) arose primarily from differences in the average thickness of the sample and stage stability during data collection. The appearance of the virus density is consistent with the reported resolution (Fig. S2d,e).

Subtomograms of spike positions – For the analysis of individual spike positions, we symmetry-expanded the virus particles from I_2 to C_1 with M (MTools, expand_symmetry). We then shifted the particle poses and corresponding reference maps and masks along x, y, and z by 132, 298, and 194 Å, respectively, thus placing the VP4 spike (in upright or reversed conformation) at the center of the new box. We then repeated the M tilt series refinement with the symmetry-expanded particles at the shifted

positions (box of 512 cubic pixels). This step allows local spike reconstructions and spike subtomograms to be identified and retrieved with specified grid samplings and box sizes.

Tomograms – Tomograms for visualization and particle picking (3D template matching) were calculated with Warp (WarpTools, ts_reconstruct) before and after tomographic tilt series refinement at 10.0 and 20.0 Å per pixel.

Merging of datasets – Table S1 lists pixel sizes that we used for processing the individual datasets. A posteriori, we determined the accurate pixel sizes for each dataset by comparing their icosahedral full virus reconstructions with the 2.36 Å cryo-EM reconstruction (EMD-45118), for which the scale had been validated by a refined atomic model with full stereochemical restraints. The errors in the processing pixel sizes were small (Table S1), and CTF correction or merging of subtomograms was not substantially affected. Because of the 100 nm-diameter rotavirus particle size, however, the errors led to small offsets of the spike subtomogram box centers among the datasets. We therefore corrected these offsets using Warp (WarpTools, shift_species) to adjust the relative box center offsets after determining shifts based on rigid body-fitted models into the spike consensus reconstruction of the individual datasets. We chose a consensus pixel size of 2.35 Å for processing of the merged subparticles from all datasets.

Metadata handling and unique particle identifiers – At each computational step, from particle picking to classification and selection of spike subparticles, we carried forward a star file with particle metadata including unique particle identifiers. After certain processing steps (e.g. after subtomogram extraction, refinement, or particle shifts), the particle poses changed, and the particle order in the default metadata files was not preserved (depending on the number of parallel jobs and order of submission during Warp/M computation). We used Python routines from Dynamo [50] to read and write star files. Python dictionaries, to lookup particle hashes, and the computation of quaternion distances (calculated from the alignment angles) helped with the non-trivial task of efficiently matching particles between Warp/M input and output files. Thus, every spike subtomogram had a unique particle identifier (dataset, tomogram, virus, spike subparticle), which allowed us to track it from the reconstructed tomogram to a final M reconstruction and 3D classification.

Spike subtomogram classification – For local classification of spike positions, we extracted 3D particles with corresponding 3D CTF volumes (132 cubic pixels, 3.2 Å per pixel) and applied a similar strategy as previously used for single particle data [4, 13, 28]. Prior to running the 3D classification in RELION, we masked each individual spike subtomogram, using a mask encompassing the volume of single VP6

and VP7 trimers, plus the volume occupied by VP5*/VP8* in upright or reversed conformation. Before applying the 3D mask to the subtomogram, the mask was transformed according to the particle alignment angles and shifts to match the subtomogram as it was extracted. The same 3D mask was then also used to mask the reference volumes during classification. Classification was carried out without alignment. We essentially obtained the same result when requesting 4, 8, or 12 classes. A first round of classification was done for each dataset (classification 1) and the result is summarized in Fig. S3. All subparticles belonging to either upright, reversed, or empty classes were merged and re-classified (classification 2), after which we obtained the following assignment for all spike positions: upright, 299,504 particles (59%); reversed, 55,972 particles (11%), empty, 158,523 particles (31%) (Fig. S4).

Supervised classification of VP7 – We made DLP and TLP masks, respectively, from the consensus RRV model (PDB-ID 9C1G, symmetry expanded to generate the full virus). For this, we selected all VP2A/B, VP6, and VP7 (in case of the TLP mask only) chains within the spike position subparticle box and made masks using a 4 Å probe radius with CCP4 [51], which were then multiplied with a 192 Å-radius spherical mask. We then masked the M reconstruction from all subparticles to generate references for DLP and TLP, respectively. Supervised classification was done in RELION with the DLP/TLP references and the TLP mask as solvent mask, for one iteration and without alignment (--iter 1 --tau2_fudge 0.2 --K 2 --ini_high 10 --skip_align). The degree of VP7 uncoating shown in Fig. 2 is per asymmetric unit of the icosahedral virus, where each of the 60 asymmetric units (containing 13 VP7 mononers each) was assigned either as VP7-occupied (TLP) or uncoated (DLP) based on the supervised classification result observed for the corresponding spike position.

Membrane segmentation – We segmented membrane in all tomograms (reconstructed at 10 Å per pixel) with MemBrain [21] using a pre-trained MemBrain segmentation model (MemBrain_seg_v10_beta) (Fig. S5a,b). For further analysis (see membrane overlap below) and display, the volumes containing the segmentation result were Fourier-sampled (for display) or local-mean binned (for membrane overlap calculation [see below]) to a pixel size of 20 Å, masked (removing membrane inside viruses, false segmentation) and dedusted (surface level 0.2, size 600) using ChimeraX [52].

Membrane overlap and distance measurements – We calculated a membrane overlap value for each spike position from the M-aligned rotavirus particles and the membrane-segmented tomograms (see above, local-mean binned to 20 Å pixel size, masked and dedusted), by counting the sum of density of segmented membrane within a 160 Å-radius mask centered at each spike position (Fig. S5d). We

applied the 160 Å-radius mask first to the membrane-segmented tomogram, converting the map to a NumPy array [53], and then taking the sum of it. We also calculated a membrane distance value for each spike position. To do so, we determined the intersection of segmented membrane with the local 3-fold axis, defined by the VP5* reversed structure (placed at each spike position regardless of its configuration). At each spike position, we cropped a box from the membrane segmentation tomograms, aligned the virtual 3-fold along the z axis, applied a cylindrical mask (5 pixel radius), and projected the density on the z axis. We detected peaks in the 1D membrane density profile using SciPy [54] (peaks with a peak height of >50% of the maximum were kept), and fitted each peak with a Gaussian. Histograms of membrane distance values for the upright and reversed spike conformation are shown in Fig. S6. For an accurate location of the membrane in case of the reversed VP5* trimer shown in Fig. 3a, we calculated the average rotational density average (RDA) from the central section of 42 viruses with extensive membrane overlap and relatively uniform close membrane contacts (Fig. 3b–c).

*Classification of membrane-engaged, reversed-conformation VP5** – From the reversed 55,972 spike subparticles, we selected 5,539 that had been assigned as TLP in the supervised VP7 classification (not uncoated), had a membrane overlap of more than 50, and a latitude of less than |±45°| (Fig. 5h). To allow classification focusing on the reversed VP5* trimer with C_3 symmetry imposed, we changed the particle alignment in the star file such that all VP5* 3-fold axes aligned and passed through the center of the box when calculating a reconstruction. We 3D classified this re-oriented particle stack in RELION (classification 3, Fig. S7).

Ribosome template matching – We template matched ribosomes in the 4×-binned tomograms (~9.40 Å per pixel) with e2spt_tempmatch.py from EMAN2 [48], using a reference prepared from an 80S structure (PDB-ID 4UG0). Particles with a score above a defined threshold (vthr 10.0) were kept, extracted as subtomograms with Warp, aligned with RELION, and refined with M (particle poses only).

Tomogram interpretation display – For the figures shown in Fig. 1d and Fig. 2 (middle column), we populated individual maps for each component (e.g. VP2A, VP2B, VP6, VP7, VP4, ribosomes) with the corresponding reference structure at the location orientations as determined from the subtomogram analysis and classification.

Liposome disruption experiment, TIRF and cryo-EM

Liposome preparation – A 2 mg total lipid mixture in chloroform of cholesterol, phosphocholine egg extract (egg PC), sphingomyelin (SM), 1,2-dioleyl-sn-glycero-3-phopshoethenolamine (DOPE), biotinylated-DOPE, Cyanine5-DOPE (Cy5-DOPE), 1-palmitoyl-2-oleyo-sn-glycerol-3-

phosphoetanolamine (POPE) and 1,2-dioleyl-sn-glycero-3-phospho-L-serine (DOPS) in molar ratio (40:22.5:10:7.25:0.5:0.25:8.5:8) was dried in a round bottom glass tube under argon gas flow. Remaining solvent was removed by incubating the lipids under high vacuum overnight. Dried lipids were resuspended in 250 µl of EDTA buffer (20 mM Tris pH 8.0, 100 mM NaCl, 1 mM EDTA) containing 2 mM carboxyfluorescein 5 and 6 dye by vortexing for two minutes, forming an 8 mg/ml lipid suspension, which was subjected to two freeze-thaw cycles with liquid nitrogen. Liposomes were then formed by extrusion with 41 passages through a 200 nm pore filter using a mini extruder (Avanti Research). The liposome suspension was loaded onto a G25 PD10 column equilibrated with TNE to separate liposomes from non-incorporated fluorophore. Fractions of 500 ul were collected.

TIRF measurements – 25 mm circular glass coverslips were cleaned and coated with a 10% (w/v) solution of biotinylated-polyethylene glycol (bio-PEG) and PEG in a ratio 1:99 (Laysan Bio, cat. no. mPEG-SCM-5000) [55] and pre-incubated with 0.5 mg/ml neutrAvidin (Thermo Scientific, cat. no. LF144746) for 15 min at room temperature (RT) before use. Liposome solutions were diluted 100 times in EDTA buffer or Ca^{2+} buffer (20 mM Tris pH 8.0, 100 mM NaCl, 1 mM EDTA) and incubated over the coverslip for 10 min at RT. Unbound liposomes were removed before imaging by several washes with EDTA or Ca^{2+} buffer. Upon addition of either EDTA buffer alone, VP7 trimer (calcium buffer) at 1.5 mg/ml, or VP7 monomer (EDTA buffer) at 1.5 mg/ml, movies were started on a Axio Observer Zeiss microscope equipped with Vector3 illumination hardware and a Photometrics Prime 95B sCMOS Camera (Teledyne, USA). Images were acquired using a Zeiss 100× 1.46 NA oil-immersion objective (Jena, Germany) with excitation from 488 and 640 nm solid-state lasers (LaserStack v4, Intelligent Imaging Innovations [3i]), both operated at 100 mW. Ring-TIRF acquisition was used through Vector3, in which the excitation beam was scanned circularly at the back focal plane of the objective during each camera exposure, producing an azimuthally averaged evanescent field at the glass–sample interface. The incident angle was set above the critical angle for total internal reflection and held constant throughout each experiment. For each field of view, we recorded 30-min movies at 1 min per frame at 50% power from each laser and 10 ms exposure at 488 nm (CF signal) and 50 ms exposure at 640 nm (Cy5-DOPE dye, liposome signal). The microscope was controlled by the SlideBook acquisition program (3i). Raw images were recorded without post-acquisition illumination correction.

Image analysis – We used previously described custom-made MATLAB (MathWorks) scripts [56] for automatic detection of fluorescent liposomes in the 640 nm channel (Cy5-DOPE dye, liposome signal) by fitting a 2D Gaussian function to diffraction-limited spots with intensities >1.5-fold above background. We extracted the XY position of each liposome at all time frames in the movie and calculated the integrated fluorescence intensity for the CF and lipid channels within a 4×4 pixel area around the XY

position. We calculated background as the integrated fluorescence intensity in a 6×6 pixel frame around the 4x4 region containing the signal, normalized the background value by area, and subtracted it from the 4×4 pixel integrated intensity. Only liposomes with detectable lipid signal at all time points were considered for analysis. Signal loss was quantified by comparing the average fluorescence of the first two time points (min 1 and 2) to the average of the final two time points (min 29 and 30) in the movie and calculating the percentage of signal loss between these two values.

Cryo-EM of liposomes incubated with VP7 – 3 µl of liposomes were incubated with 15 µl of VP7 (1.5 mg/ml) or $VP7^{292-312}$ peptide (synthetized by TUCF Peptide Synthesis) at room temperature for 30 min. 4 µl of the sample was then placed on a glow-discharged 1.2/1.3 Quantifoil grid, blotted for 6 s at 90% humidity and plunge frozen in liquid ethane in a Vitrobot (Thermo-Fischer). Grids were stored in liquid nitrogen until imaging. Micrographs of liposomes were recorded on a Thermo Fisher Scientific Talos Arctica equipped with a Gatan K3 detector at a pixel size of 1.44 A^2 with a total dose of 50 electrons/$Å^2$ at a defocus of -2.0 to -2.5 µm. SerialEM version 4.2.12 was used for data acquisition [57].

Infectivity assays

Infectivity assay of TLPs – Focus-forming unit (FFU) concentrations for TLP were determined by infectious focus assays as previously described [58]. Specific infectivity was calculated by normalizing FFU titers to particle concentrations determined by densitometry of Coomassie blue-stained SDS-PAGE gels. For the experiments with Latrunculin A (Lat A), cells were incubated for 1 hour with 5 µM Lat A, which was diluted in Dulbecco's Modified Eagle's Medium (DMEM, Thermo Fisher Scientific) from a 1 mM stock solution in dimethyl sulfoxide (DMSO). BSC-1 cells, grown overnight in a 96-well plate, were washed with DMEM and inoculated with serial dilutions of trypsin activated virus in DMEM containing 5 µM Lat A and 1 µg/ml trypsin. For the assays testing trypsin inhibitor, cells were washed and inoculated with serial dilutions of trypsin activated virus in presence of either 1 µg/ml trypsin or 1 µg/ml Defined Trypsin Inhibitor (Gibco). After 1 h at 37 °C incubation with virus particles, the inoculum was removed and replaced with DMEM containing 10% fetal bovine serum and 2.5 µg/ml neutralizing monoclonal antibody M159 to prevent secondary infection. At 16 h post-infection, cells were washed with phosphate-buffered saline (PBS) and fixed with methanol. Infectious FFUs were detected by immunoperoxidase staining using monoclonal antibody M60 (anti-VP7) as the primary detection antibody, and peroxidase labeled Goat anti-Mouse IgG (SeraCare) as secondary antibody. Once developed, FFU were counted by light microscopy.

GCaMP live-cell fluorescence microscopy experiments

Cell culture and transfection – BSC-1 cells were plated on glass-bottom 18-well dishes at 70% confluence and allowed to adhere overnight in DMEM Glutamax, supplemented with 10% Hi-FBS (Thermo Fisher Scientific). The following day, cells were transiently transfected with plasmid DNA (Addgene plasmid # 52228 -- pGP-CMV-GCaMP6s-CAAX, a gift from Tobias Meyer.) using Lipofectamine 2000 (Thermo Fisher Scientific). Briefly, plasmid DNA and Lipofectamine 2000 were diluted separately in antibiotic-free OPTI-MEM, combined, and incubated for 20 min to allow complex formation before addition to cells. Cells were incubated with transfection complexes for 6 h, after which the medium was replaced with fresh DMEM Glutamax, supplemented with 10% FBS. Cells were then allowed to recover and express the transgene overnight.

Labeling of TLPs – TLPs were diluted to a final concentration of 1.0 mg/ml in a total volume of 60 µl using HNC buffer (20 mM HEPES, pH 8.0, 100 mM NaCl, 1 mM $CaCl_2$). Subsequently, 6.7 µl of 1 M $NaHCO_3$ (pH 8.3) was added, followed by 1.9 µl of 0.0076 mg/ml Atto 565 NHS ester and incubated for 1 h at room temperature. The reaction was quenched by addition of 5 µl of 1 M Tris (pH 8.0). Labeled particles were buffer exchanged into 20 mM Tris (pH 8.0), 100 mM NaCl, and 1 mM $CaCl_2$ using Zeba Spin Desalting Columns (Thermo Fisher Scientific).

Confocal microscopy and live-cell imaging – Labeled TLPs were added to cells at a final concentration of 0.030 mg/ml and incubated during 5 min before starting imaging. Movies of 10 minutes with a time-lapse interval of 10 s were acquired using a Zeiss Axio Observer Z1 inverted microscope equipped with environmental control (37 °C, 5% CO_2) and a CSU-X1 spinning disk confocal unit (Yokogawa), operated by the Marianas (3i) platform. The system included a spherical aberration correction module and a 3i LaserStack with diode lasers at 488, 561 (150 mW), and 640 nm (100 mW). Emission was filtered using 525/40, 609/54, and 692/40 filters (Semrock). Single plane movies were acquired with 50 ms exposure using a dual-camera sCMOS system (Prime 95B, Teledyne Photometrics) and a 40X objective. Final XY resolution was 0.22×0.22 µm/pixel. Background intensity was subtracted using Fiji [59] and fluorescence intensity of the GCaMP signal in in the cell was plotted as a function of time.

Figure preparation

Figures were prepared with PyMOL (The PyMOL Molecular Graphics System, Version 2.3 Schrödinger, LLC), ChimeraX [52], Fiji, and matplotlib [60].

Data availability

The cryo-ET maps from subtomogram averaging are deposited in the Electron Microscopy Data Bank with accession identifiers EMD-75185 (icosahedral virus reconstruction from dataset 2, Fig. S2) and

EMD-75186 (membrane-bound, reversed VP5* trimer, classification 3 with a tight mask, class 1, Fig. 3a and Fig. S7). Atomic coordinates are deposited in the Protein Data Bank with accession identifiers PDB-ID 10IC (icosahedral virus) and PDB-ID 10ID (reversed VP5* trimer).

ACKNOWLEDGMENTS

We thank the staff at the Harvard Medical School Center for Cryo-Electron Microscopy in Structural Biology, for expert advice and assistance, and Eric Marino and members of the Kirchhausen laboratory (Boston Children's Hospital), for assistance with fluorescence microscopy. The work was supported by NIH grants R01 CA13202 (to SCH), R35 GM139386 (to TK), and R01 AI163019 (to TK and Sean Whelan, Washington University in St. Louis). SCH is an Investigator in the Howard Hughes Medical Institute.

AUTHOR CONTRIBUTIONS. Conceptualization: all authors. Experimental design and data collection: MdS and CL. Data analysis and computational interpretation: MdS and SJ. Drafting the MS: MdS, SJ, SCH. Editing the MS: all authors.

The authors declare no competing interests

FIGURE CAPTIONS

Fig. 1. In situ visualization of rotavirus cell entry by cryo-ET.
a, Structure of a rotavirus particle, partially cut open to expose internal structures. Viral subunits are shown in surface representation. VP2 (VP2A and VP2B, in blue and cyan, respectively) and VP6 (green) form the shell of the “double-layer” particle (DLP), packaging the viral RNA, VP1 (gray, the capsid-bound RNA-dependent RNA polymerases [RdRp]), and VP3 (not shown, the RNA cap-generating enzyme). The outer layer of the “triple-layer” particle (TLP) contains VP7 (yellow) and VP4, proteolytically cleaved to VP8* (magenta) and VP5* (red, orange, and salmon). **b,** Upright (PDB-ID 9C1H) and reversed (PDB-ID 9C1J) conformations of VP4, after cleavage to VP8* (magenta) and VP5* (red, orange, salmon). Foot regions of reversed conformation shown schematically in gray. **c**, Cryo-SEM image of BSC-1 cells deposited on the carbon film of a gold mesh and vitrified for tomography. **d,** Molecular interpretation (segmentation) of a representative tomogram of a BSC-1 cell incubated with rotavirus. The plasma membrane is indicated by a dashed line. The inset shows a side view of the tomogram with its approximate dimensions. See Methods for description of segmentation procedure. See Movie S1 for the raw reconstructed tomogram and segmentation.

Fig. 2. Rotavirus cell entry steps.

a–f, Left-hand column: two representative 10 nm-thick tomogram sections centered on particles of interest. Scale bars: 100 nm. ***Central column***: molecular interpretation of the two tomogram sections shown on the left. Particles are positioned and oriented as determined from the subtomogram analysis, with VP6 (green), VP7 (yellow), VP5*/VP8* in upright conformation (light red), and VP5* in reversed conformation (dark red). Segmented membranes are shown in gray, ribosomes in beige. For each particle, an inset shows the extent of VP7 uncoating on a viral surface projection and by a horizonal bar plot (t/d = TLP / DLP); the number and conformation of spikes in upright (light red) and reversed (dark red) conformation (u/r/e = upright / reversed / empty); the total volume of segmented membrane within a 16-nm sphere drawn at each spike position (m = membrane); and the number of ribosomes in the vicinity of the particle (80S = ribosomes). ***Right-hand column***: interpretative sketch. **a,** Attachment of TLP to host cell. **b,** Invagination of cell membrane and particle uptake. **c,** Membrane permeabilization induced by VP5* bilayer interaction and conformational change from upright (light red) to reversed (dark red), resulting in loss of Ca^{2+} from the endocytic vesicle. **d,** Membrane perforation by dissociated VP7. **e,** DLP release into the cytosol. **f,** Synthesis and extrusion of viral mRNA and potential translation of emerging transcripts.

Fig. 3. Membrane interaction of VP5.

a, Structure of membrane-bound, reversed VP5*. Subtomogram average density of 3,255 reversed spikes obtained after classification (C_3 symmetry imposed) in gray. The rotavirus reversed VP5* model (PDB-ID 9C1J) was placed into the density and is colored as in Fig. 1. VP5* foot domain density is labeled. The middle of the membrane (dotted line), as determined from the radial density profile shown in (**d**). The thickness of the membrane is shown by the approximate position of the lipid head groups (gray bands). The close-up shows the hydrophobic loops at the tip of the β-barrel domains with amino acid residues labeled. **b,** Icosahedrally averaged density from 42 rotavirus particle subtomograms where most spikes were observed in close contact with membrane. RNA, gray; VP2A, VP2B, blue and cyan, respectively; VP6, green; VP7 yellow; VP5*, red, orange, and salmon; membrane, gray. **c,** Radial density profile (RDA) in arbitrary units (AU), calculated from 42 rotavirus subtomograms averaged to generate the figure in (**b**) (see Methods for details). The peak corresponding to the VP7 layer is labeled. Membrane appears as a double peak. The middle of the lipid bilayer is 443 Å from the center of the virus and marked with a dotted line.

Fig. 4. Membrane perforation by VP7 monomer.

a, Schematic of the total internal reflection fluorescence (TIRF) microscopy experimental set-up: carboxyfluorescein (CF, green)-containing liposomes with biotinylated-DOPE and Cy5-DOPE (magenta) are tethered to a biotinylated-PEG coated coverslip by neutravidin. **b,** Time-lapse TIRF microscopy imaging of liposomes incubated with VP7 trimer (Ca^{2+} buffer, top row) or VP7 monomer (EDTA buffer, bottom row) and imaged at indicated time points. CF-channel is shifted 7 pixels to the right from lipid-channel for better colocalization visualization. **c,** Quantification of liposome permeabilization showing the percentage of liposomes with signal loss of more than 50% after 30 min incubation with buffer only (white), VP7 trimer (light grey) or VP7 monomer (dark grey). Error bars represent the standard error of the mean (SEM, n = 3 independent experiments) and t-test statistical analysis was used between samples. *, $p < 0.05$; **, $p < 0.01$; ns, not significant. **d,** Cryo-EM images of perforated liposomes after 30 min incubation with VP7 monomer or $VP7^{292–312}$ peptide. **e,** Schematic diagram, based on Figs. 2d and 2e, representing perforations seen in viral uptake vesicles, for comparison with the images in (d) of liposomes incubated with VP7 monomer. **f,** VP7 trimer (PDB-ID 9C1G [3]) highlighting the C-terminal amphipathic helix (residues 292–312, orange). The VP7 monomer (yellow, center) shows domains I and II, with the C-terminal helix extending from the bipartite globular body of the protein. Helical wheel projection of residues 292–312, showing segregation of hydrophobic (orange) and hydrophilic (gray) residues. The sequence below shows the amphipathic region (orange) and adjacent residues in the C terminus.

SUPPLEMENTARY FIGURE CAPTIONS

Fig. S1. Cryo-ET sample preparation workflow for rotavirus infected BSC-1 cells.
a, Sample preparation protocol. BSC-1 cells were seeded on gold EM grids and incubated overnight. **b, c,** Cells were infected with rotavirus during 10 min and incubated with medium for another 10 min, then back-blotted and plunge-frozen in liquid ethane. **d,** Representative scanning electron micrograph (SEM) of vitrified BSC-1 cells on a grid square, acquired on an Aquilos cryo-SEM. Ice quality was evaluated by assessing cell morphology and ice thickness. **e,** Low-magnification images were acquired on an Aquilos (scanning electron microscopy: SEM, left) and Krios (transmission electron microscopy: TEM, center) to evaluate the quality and quantity of cells on the grid. Insets show higher magnification views of selected cells. **f,** Medium-magnification TEM image montage of a BSC-1 cell on a grid square. The magenta outline shows the cell membrane boundary and suitable regions for tomogram acquisition. **g,** High-magnification TEM image showing the quality of cellular preservation with clearly visible membrane bilayers and intracellular structures suitable for cryo-ET.

Fig. S2. Icosahedral (I_2) rotavirus (RRV) reconstructions from subtomograms.

a, Determination of the true pixel size for each dataset (Table S1) using a 2.36 Å resolution cryo-EM RRV map (EMD-45118) as reference. Map correlation coefficients (CC) were calculated between differently scaled subtomogram reconstructions and the reference map. The scale factors corresponding to the true pixel size are highlighted with an arrow. **b,** Fourier shell correlation (FSC) curves calculated from the final M reconstruction half maps for each of the 7 datasets. Maps were scaled to the true pixel sizes (Table S1, Fig. S2a). The number of particles is given in parenthesis. The conventional cutoff of 0.143 for meaningful half map correlation is indicated. Nyquist frequency corresponds to 4.7 Å. **c,** FSC curves calculated from the final M reconstruction map and a 2.36 Å high-resolution cryo-EM RRV map (EMD-45118), serving as "model". Maps were scaled to the true pixel sizes (Table S1, Fig. S2a). The conventional cutoff of 0.5 for meaningful map-model correlation is indicated. Nyquist frequency corresponds to 4.7 Å. **d,** Dataset 2 I_2 RRV reconstruction, filtered and colored according to local resolution, at increasing contour level from left to right. **e,** Close-up view of the VP2A/VP2B inner layer density (dataset 2, M-sharpened map) showing molecular features (helical groves and appearance of bulky side chains) consistent with a 4.7 Å-resolution map.

Fig. S3. 3D classification 1 of spike positions.

For each of the 7 datasets, 3D classification 1 was done with RELION, and maps shown here were reconstructed with M (see Methods). For each class, the number of subparticles and the percentage of the total number of particles is given. Spike position configuration is color coded for each class: upright, light red; reversed, dark red; empty (unoccupied, no VP4 present), gray.

Fig. S4. 3D classification 2 of spike positions.

After merging upright, reversed, and empty classes (Fig. S3) from each dataset, 3D classification 2 was done with RELION, and maps shown here were reconstructed with M (see Methods). Spike position configuration is color coded: upright, light red; reversed, dark red; empty (unoccupied, no VP4 present), gray. 3D classification 2, the particles partitioned into 299k upright, 56k reversed, and 159k empty spike positions.

Fig. S5. Overlap of spike positions with segmented membrane

a, Overview of the steps performed to calculate the overlap between spike location and segmented membrane. **b,** Membrane segmentation result for a representative tomogram, viewed along the optical axis of the microscope (left) and from the side (right). **c,** Histogram showing the distribution of total detected membrane volume per tomogram. **d,** Illustration how the overlap between spike location and segmented membrane was calculated for each spike position. The membrane overlap is defined as the volume of segmented membrane within a sphere centered at the spike position with a radius of 160 Å.

e, Histogram showing the distribution of total membrane overlap per virus in arbitrary units (AU). Particles with the highest values were false template matching picks. **f,** Representative examples rotaviruses with high membrane overlap (extend close membrane contacts), shown as 10-nm thick tomographic slices (top row, scale bar = 100 nm) with the corresponding tomogram interpretations (bottom row). **g–j,** Violin plots showing the distribution of membrane overlap in arbitrary units (AU) for upright and reversed spikes (bottom row). The number of spikes is given in parenthesis. The black bar is the mean of the distribution. ***, $p < 0.001$. Distribution of the spikes on the viral surface included in the analysis (top row). In panels g and i, all spike positions were included. In panels, h and j, spikes with high latitude were excluded, because the missing wedge in Fourier space leads to essentially undetectable membrane (when oriented perpendicular to the optical axis of the microscope) for those spikes. **g,** Analysis for all tomograms and all upright and reversed spikes. **h,** Analysis for all tomograms and spikes with latitude smaller than |±45°|. **i,** Analysis for a single tomogram and all upright and reversed spikes. **j,** Analysis for a single tomograms and spikes with latitude smaller than |±45°|.

Fig. S6. Membrane distance histograms.

Distance between the virus center and segmented membrane (see Methods for details). **a,** Calculated for 37,702 upright VP5*/VP8* spikes. **b,** Calculated for 8,518 reversed VP5* spikes.

Fig. S7. 3D classification 3 of a selected (high membrane overlap) set of VP5* reversed spikes.

3D classification 3 was done with RELION without alignment and C_3 symmetry imposed, and maps shown here were reconstructed with M and filtered according to local resolution (see Methods). Top, classification with a wide mask. Bottom, classification with a tight mask. Spike position configuration is color coded: reversed, dark red; empty (unoccupied, no VP4 present), gray. The map of class 1 obtained after classification with a tight mask is shown in Fig. 3a.

Fig. S8. Rotavirus induces localized calcium transients in BSC1 cells.

a. GCaMP fluorescence intensity over time in a representative BSC1 cell after 5 min incubation with rotavirus. Arrows indicate transient calcium spikes. **b.** Confocal microscopy images corresponding to the different timepoints indicated with gray arrows in (a). GCaMP calcium indicator is shown in yellow and fluorescently labeled rotavirus in magenta. White arrowheads indicate regions of elevated GCaMP fluorescence corresponding to calcium transients. Inset shows magnified view of both channels separately in a region of the cell. Scale bar, 10 µm. **c.** GCaMP fluorescence intensity over time in a representative uninfected control BSC1 cell showing stable baseline calcium levels. **d.** Time-lapse images of the control cell shown in (c). Scale bar, 10 µm.

Fig. S9. Actin reorganization at rotavirus entry sites.

a, Rotavirus infectivity in the absence (control, black circles) or presence (gray squares) of 1 μM latrunculin A, an actin polymerization inhibitor. Data represent the mean ± standard deviation from three independent experiments. **b–e,** Representative tomographic slices of rotavirus-infected BSC-1 cells showing viruses close to cytoskeletal networks. Branched actin networks surround entering virus particles. The scale bar corresponds to 100 nm (panel d). **f,** Manual segmentation of actin filaments (green) surrounding a rotavirus particle. Dashed boxes indicate the regions shown in higher detail. **g,** Serial tomographic slices along the z axis of the same virus particle shown in panel f.

Fig. S10. Quantification of TIRF microscopy data.

a–c, Percentage of liposomes with carboxyfluorescein (CF) signal loss greater than 50% after 30 min incubation with EDTA buffer only (white bars), VP7 trimer in Ca^{2+} buffer (light grey bars), and VP7 monomer in EDTA buffer (dark grey bars), for three independent experiments (a, b and c). Total number of liposomes is shown at the bottom of each bar. Error bars represent the standard error of the mean (SEM, n = 3 independent experiments); Two sided t-test statistical analysis was used between samples. *, $p < 0.05$; **, $p < 0.01$; ***, $p < 0.001$; ns, not significant. **d**, Liposome signal loss (%) for all liposomes in the three independent experiments. Total number of liposomes per condition (n) is shown for each sample. **e, f,** The red dotted line indicates the cut off of 50%. Percentage of liposomes with signal loss of more than 50% (e) or 80% (f) after 30 min incubation with EDTA buffer only (white bar), VP7 trimer in Ca^{2+} buffer (light grey bar) or VP7 monomer (dark grey bar). Plotted data are from three independent experiments. Total number of liposomes (n) is shown for each condition. Error bars represent the standard error of the mean (SEM, n = 3 independent experiments); t-test statistical analysis was used between samples, with p values indicated.

Fig. S11. cryo-EM of VP7-disrupted liposomes.

a–d, Representative cryo-EM micrographs of liposomes after 30 min incubation with VP7 monomer in EDTA buffer. White arrows show perforation of the liposomes. Scale bar, 500 Å.

Fig. S12. Infectivity assay of virus particles incubated with trypsin inhibitor

a, The table shows the infectivity values as focus-forming units per milliliter (FFU/ml) for the TLP sample and TLP incubated with trypsin inhibitor for three independent experiments, determined as described in Methods. **b,** The average and standard deviation (Std Dev) of the three independent experiments are displayed in a bar graph with the focus-forming unit concentration (FFU/ml) for TLPs in white and TLPs incubated with trypsin inhibitor in gray. A t-test statistical analysis was performed (p value = 0.4; ns, not significant).

SUPPLEMENTARY MOVIES

Movie S1. 3D movie of the reconstructed tomogram corresponding to Fig. 1d.

The movie shows the raw reconstructed tomogram viewed along the Z axis. The segmented membrane is rendered in gray, ribosomes in beige, and rotavirus proteins are shown as follows: VP2A and VP2B in blue and cyan, respectively; VP6 in green; VP7 in yellow; and surface spikes in the upright (light red) and reversed (dark red) conformations.

SUPPLEMENTARY TABLES

Table S1. Cryo-ET data collection and tilt series refinement.

SUPPLEMENTARY DATA

Data S1. Overlap of spike positions with segmented membrane for each tomogram.

Violin plots showing the distribution of membrane overlap in arbitrary units (AU) for upright and reversed spikes for each tomogram containing rotavirus (537 tomograms). The number of spikes is given in parenthesis. The black bar is the mean of the distribution. Only spikes with latitude smaller than |±45°| were included in the analysis (see also Fig. S5g–i). The inset horizonal bar plot shows the total detected membrane volume for each tomogram.

REFERENCES

1. Crawford, S., et al., *Rotaviruses*, in *Fields Virology, 7th ed.*, P.M. Howley and D.M. Knipe, Editors. 2023, Wolters Kluyver: Philadelphia, PA. p. 362-413.

2. Settembre, E.C., et al., *Atomic model of an infectious rotavirus particle.* EMBO J, 2011. **30**(2): p. 408-16.

3. Aoki, S.T., et al., *Structure of rotavirus outer-layer protein VP7 bound with a neutralizing Fab.* Science, 2009. **324**(5933): p. 1444-7.

4. Herrmann, T., et al., *Functional refolding of the penetration protein on a non-enveloped virus.* Nature, 2021. **590**(7847): p. 666-670.

5. Lu, X., et al., *Mechanism for coordinated RNA packaging and genome replication by rotavirus polymerase VP1.* Structure, 2008. **16**(11): p. 1678-88.

6. Bartlett, N.M., et al., *Electron microscopy study of reovirus reaction cores.* J Virol, 1974. **14**(2): p. 315-26.

7. Lawton, J.A., M.K. Estes, and B.V. Prasad, *Three-dimensional visualization of mRNA release from actively transcribing rotavirus particles.* Nat Struct Biol, 1997. **4**(2): p. 118-21.

8. Jenni, S., et al., *In situ Structure of Rotavirus VP1 RNA-Dependent RNA Polymerase.* J Mol Biol, 2019. **431**(17): p. 3124-3138.

9. Ding, K., et al., *In situ structures of rotavirus polymerase in action and mechanism of mRNA transcription and release.* Nat Commun, 2019. **10**(1): p. 2216.

10. Dormitzer, P.R., et al., *Specificity and affinity of sialic acid binding by the rhesus rotavirus VP8* core.* J Virol, 2002. **76**(20): p. 10512-7.

11. Hu, L., et al., *Cell attachment protein VP8* of a human rotavirus specifically interacts with A-type histo-blood group antigen.* Nature, 2012. **485**(7397): p. 256-9.

12. Abdelhakim, A.H., et al., *Structural correlates of rotavirus cell entry.* PLoS Pathog, 2014. **10**(9): p. e1004355.

13. de Sautu, M., et al., *The rotavirus VP5*/VP8* conformational transition permeabilizes membranes to Ca2.* PLoS Pathog, 2024. **20**(4): p. e1011750.

14. Kaljot, K.T., et al., *Infectious rotavirus enters cells by direct cell membrane penetration, not by endocytosis.* J Virol, 1988. **62**(4): p. 1136-44.

15. Salgado, E.N., et al., *Visualization of Calcium Ion Loss from Rotavirus during Cell Entry.* J Virol, 2018. **92**(24): p. e01327-18.

16. Salgado, E.N., S. Upadhyayula, and S.C. Harrison, *Single-particle detection of transcription following rotavirus entry.* J Virol, 2017: p. e00651-17.

17. Dormitzer, P.R., H.B. Greenberg, and S.C. Harrison, *Purified recombinant rotavirus VP7 forms soluble, calcium-dependent trimers.* Virology, 2000. **277**(2): p. 420-8.

18. Galaz-Montoya, J.G., et al., *Single particle tomography in EMAN2.* J Struct Biol, 2015. **190**(3): p. 279-90.

19. Burt, A., et al., *An image processing pipeline for electron cryo-tomography in RELION-5.* FEBS Open Bio, 2024. **14**(11): p. 1788-1804.

20. Tegunov, D., et al., *Multi-particle cryo-EM refinement with M visualizes ribosome-antibiotic complex at 3.5 A in cells.* Nat Methods, 2021. **18**(2): p. 186-193.

21. Lamm, L., et al., *MemBrain: A deep learning-aided pipeline for detection of membrane proteins in Cryo-electron tomograms.* Comput Methods Programs Biomed, 2022. **224**: p. 106990.

22. Lamm, L., et al., *MemBrain v2: an end-to-end tool for the analysis of membranes in cryo-electron tomography.* bioRxiv, 2024: p. 2024.01.05.574336.

23. Dormitzer, P.R., et al., *Structural rearrangements in the membrane penetration protein of a non-enveloped virus.* Nature, 2004. **430**(7003): p. 1053-8.

24. Tsai, F.C., et al., *A polarized Ca2+, diacylglycerol and STIM1 signalling system regulates directed cell migration.* Nat Cell Biol, 2014. **16**(2): p. 133-44.

25. Trask., S.D., *The Mechanism of Membrane Penetration by Rotavirus*, in *Division of Medical Sciences*. 2008, Harvard University.

26. Elaid, S., et al., *A peptide derived from the rotavirus outer capsid protein VP7 permeabilizes artificial membranes.* Biochim Biophys Acta, 2014. **1838**(8): p. 2026-35.

27. Massol, R.H., et al., *A burst of auxilin recruitment determines the onset of clathrin-coated vesicle uncoating.* Proc Natl Acad Sci U S A, 2006. **103**(27): p. 10265-10270.

28. Jenni, S., et al., *Rotavirus VP4 Epitope of a Broadly Neutralizing Human Antibody Defined by Its Structure Bound with an Attenuated-Strain Virion.* J Virol, 2022. **96**(16): p. e0062722.

29. Aoki, S.T., et al., *Cross-linking of rotavirus outer capsid protein VP7 by antibodies or disulfides inhibits viral entry.* J Virol, 2011. **85**(20): p. 10509-17.

30. Cohen, J., et al., *Activation of rotavirus RNA polymerase by calcium chelation.* Arch Virol, 1979. **60**(3-4): p. 177-86.

31. Rossjohn, J., et al., *Structures of perfringolysin O suggest a pathway for activation of cholesterol-dependent cytolysins.* J Mol Biol, 2007. **367**(5): p. 1227-36.

32. Shai, Y., *Mechanism of the binding, insertion and destabilization of phospholipid bilayer membranes by alpha-helical antimicrobial and cell non-selective membrane-lytic peptides.* Biochim Biophys Acta, 1999. **1462**(1-2): p. 55-70.

33. Niitsu, A., et al., *Rational Design Principles for De Novo alpha-Helical Peptide Barrels with Dynamic Conductive Channels.* J Am Chem Soc, 2025. **147**(14): p. 11741-11753.

34. Yang, L., et al., *Barrel-stave model or toroidal model? A case study on melittin pores.* Biophys J, 2001. **81**(3): p. 1475-85.

35. Gillies, L.A., et al., *Visual and functional demonstration of growing Bax-induced pores in mitochondrial outer membranes.* Mol Biol Cell, 2015. **26**(2): p. 339-49.

36. Kuwana, T., et al., *Pro-apoptotic Bax molecules densely populate the edges of membrane pores.* Sci Rep, 2016. **6**: p. 27299.

37. Zhang, Y., et al., *Structural basis of BAX pore formation.* Science, 2025. **388**(6754): p. eadv4314.

38. Czabotar, P.E. and A.J. Garcia-Saez, *Mechanisms of BCL-2 family proteins in mitochondrial apoptosis.* Nat Rev Mol Cell Biol, 2023. **24**(10): p. 732-748.

39. Greber, U.F., et al., *Stepwise dismantling of adenovirus 2 during entry into cells.* Cell, 1993. **75**(3): p. 477-86.

40. Maier, O., et al., *An N-terminal domain of adenovirus protein VI fragments membranes by inducing positive membrane curvature.* Virology, 2010. **402**(1): p. 11-9.

41. Moyer, C.L., et al., *Functional genetic and biophysical analyses of membrane disruption by human adenovirus.* J Virol, 2011. **85**(6): p. 2631-41.

42. Wiethoff, C.M. and G.R. Nemerow, *Adenovirus membrane penetration: Tickling the tail of a sleeping dragon.* Virology, 2015. **479-480**: p. 591-9.

43. Greenberg, H.B., et al., *Production and preliminary characterization of monoclonal antibodies directed at two surface proteins of rhesus rotavirus.* J Virol, 1983. **47**(2): p. 267-75.

44. Hagen, W.J.H., W. Wan, and J.A.G. Briggs, *Implementation of a cryo-electron tomography tilt-scheme optimized for high resolution subtomogram averaging.* J Struct Biol, 2017. **197**(2): p. 191-198.

45. Tegunov, D. and P. Cramer, *Real-time cryo-electron microscopy data preprocessing with Warp.* Nat Methods, 2019. **16**(11): p. 1146-1152.

46. Mastronarde, D.N. and S.R. Held, *Automated tilt series alignment and tomographic reconstruction in IMOD.* J Struct Biol, 2017. **197**(2): p. 102-113.

47. Zheng, S., et al., *AreTomo: An integrated software package for automated marker-free, motion-corrected cryo-electron tomographic alignment and reconstruction.* J Struct Biol X, 2022. **6**: p. 100068.

48. Chen, M., et al., *A complete data processing workflow for cryo-ET and subtomogram averaging.* Nat Methods, 2019. **16**(11): p. 1161-1168.

49. Scheres, S.H., *RELION: implementation of a Bayesian approach to cryo-EM structure determination.* J Struct Biol, 2012. **180**(3): p. 519-30.

50. Castano-Diez, D., et al., *Dynamo: a flexible, user-friendly development tool for subtomogram averaging of cryo-EM data in high-performance computing environments.* J Struct Biol, 2012. **178**(2): p. 139-51.

51. Agirre, J., et al., *The CCP4 suite: integrative software for macromolecular crystallography.* Acta Crystallogr D Struct Biol, 2023. **79**(Pt 6): p. 449-461.

52. Pettersen, E.F., et al., *UCSF ChimeraX: Structure visualization for researchers, educators, and developers.* Protein Sci, 2021. **30**(1): p. 70-82.

53. Harris, C.R., et al., *Array programming with NumPy.* Nature, 2020. **585**(7825): p. 357-362.

54. Virtanen, P., et al., *SciPy 1.0: fundamental algorithms for scientific computing in Python.* Nat Methods, 2020. **17**(3): p. 261-272.

55. Kyoung, M., et al., *Studying calcium-triggered vesicle fusion in a single vesicle-vesicle content and lipid-mixing system.* Nat Protoc, 2013. **8**(1): p. 1-16.

56. Cocucci, E., et al., *The first five seconds in the life of a clathrin-coated pit.* Cell, 2012. **150**(3): p. 495-507.

57. Mastronarde, D.N., *SerialEM: A Program for Automated Tilt Series Acquisition on Tecnai Microscopes Using Prediction of Specimen Position.* Microscopy and Microanalysis, 2003. **9**(S02): p. 1182-1183.

58. Trask, S.D. and P.R. Dormitzer, *Assembly of highly infectious rotavirus particles recoated with recombinant outer capsid proteins.* J Virol, 2006. **80**(22): p. 11293-304.

59. Schindelin, J., et al., *Fiji: an open-source platform for biological-image analysis.* Nat Methods, 2012. **9**(7): p. 676-82.

60. Hunter, J.D., *Matplotlib: A 2D graphics environment.* Comput. Sci. Eng., 2007. **9**(3): p. 90-5.

Fig. 1

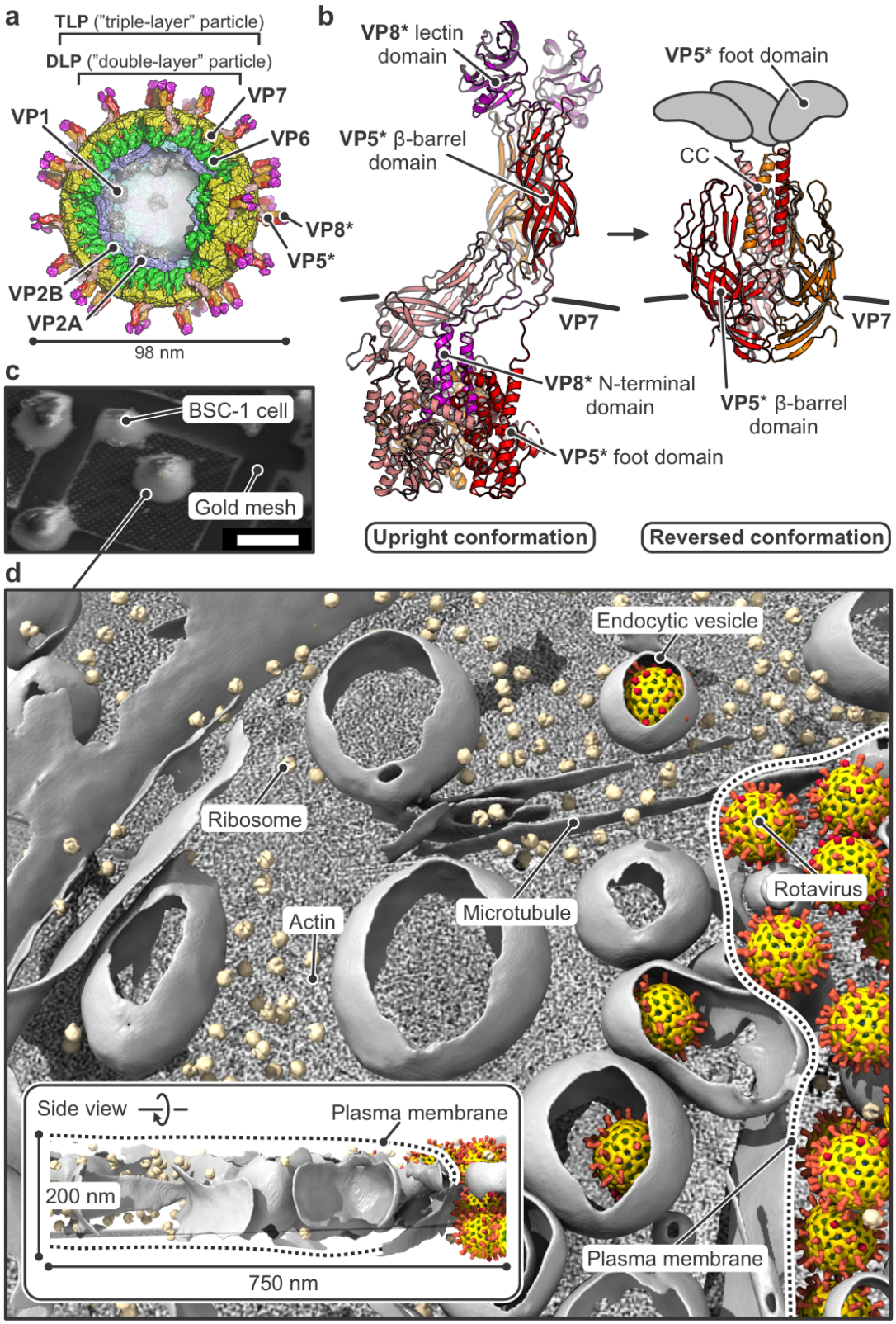
a
TLP ("triple-layer" particle)
DLP ("double-layer" particle)
VP1
VP7
VP6
VP8*
VP5*
VP2B
VP2A
98 nm
b
VP8* lectin domain
VP5* β-barrel domain
VP5* foot domain
CC
VP7
VP7
VP8* N-terminal domain
VP5* β-barrel domain
VP5* foot domain
Upright conformation
Reversed conformation
c
BSC-1 cell
Gold mesh
d
Endocytic vesicle
Ribosome
Rotavirus
Microtubule
Actin
Side view
Plasma membrane
200 nm
750 nm
Plasma membrane

Fig. 2

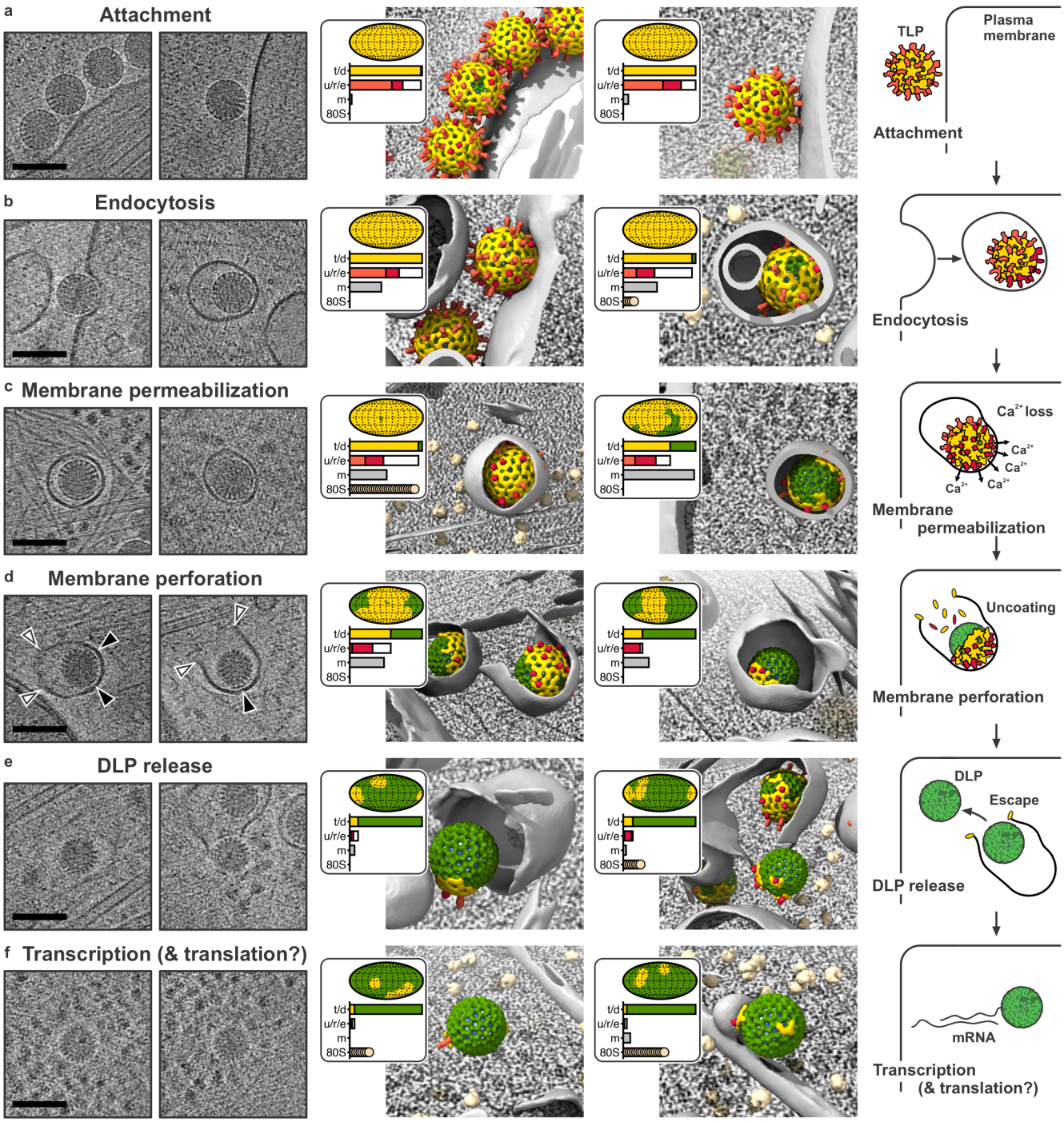
a
Attachment
b
Endocytosis
c
Membrane permeabilization
d
Membrane perforation
e
DLP release
f
Transcription (& translation?)
t/d
u/r/e
m
80S
TLP
Plasma membrane
Attachment
Endocytosis
Ca2+ loss
Membrane permeabilization
Uncoating
Membrane perforation
DLP
Escape
DLP release
mRNA
Transcription (& translation?)

Fig. 3

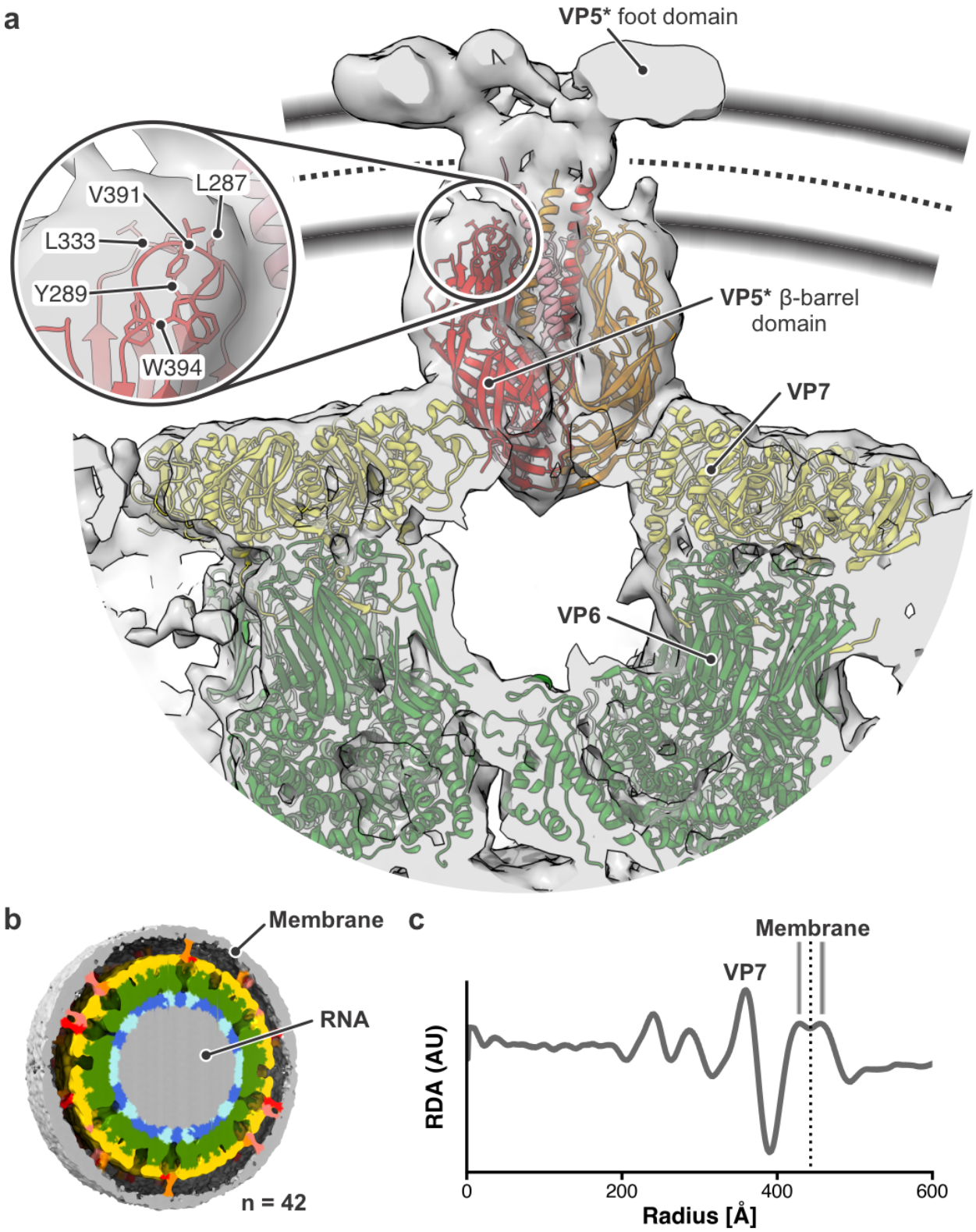
a
VP5* foot domain
V391
L287
L333
Y289
W394
VP5* β-barrel domain
VP7
VP6
b
Membrane
RNA
n = 42
c
Membrane
VP7
RDA (AU)
0
200
400
600
Radius [Å]

Fig. 4

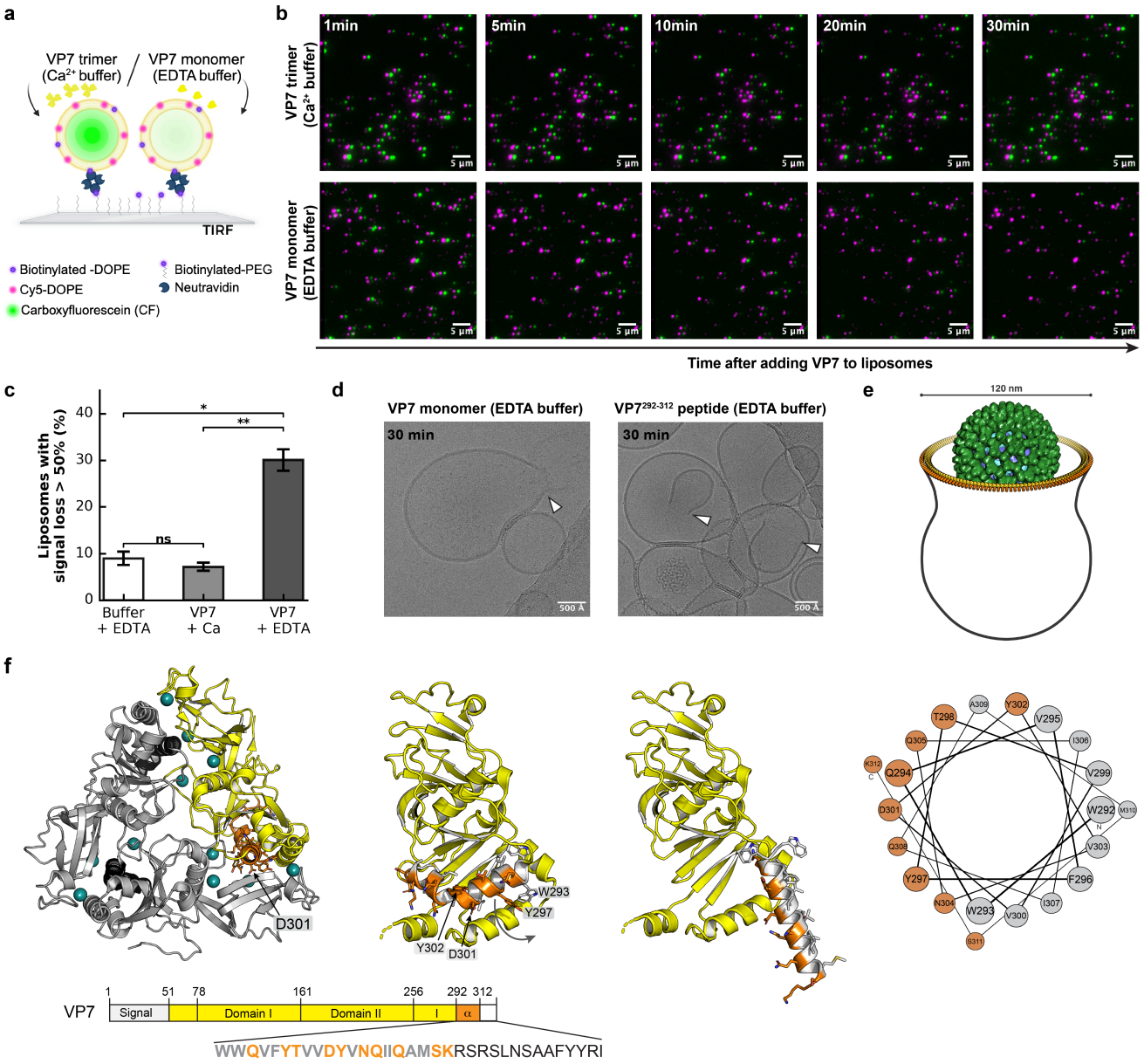
a
VP7 trimer (Ca2+ buffer)
VP7 monomer (EDTA buffer)
TIRF
Biotinylated -DOPE
Cy5-DOPE
Carboxyfluorescein (CF)
Biotinylated-PEG
Neutravidin
b
1min
5min
10min
20min
30min
VP7 trimer (Ca2+ buffer)
VP7 monomer (EDTA buffer)
5 µm
Time after adding VP7 to liposomes
c
Liposomes with signal loss > 50% (%)
ns
*
**
Buffer + EDTA
VP7 + Ca
VP7 + EDTA
d
VP7 monomer (EDTA buffer)
VP7292-312 peptide (EDTA buffer)
30 min
500 Å
e
120 nm
f
D301
W293
Y297
Y302
VP7
Signal
Domain I
Domain II
WWQVFYTVVDYVNQIIQAMSKRSRSLNSAAFYYRI